Initial State Interaction for the ^{20}Ne + ^{130}Te and ^{18}O + ^{116}Sn Systems at 15.3 AMeV from Elastic and Inelastic Scattering Measurements

Diana Carbone [1,*], Roberto Linares [2], Paulina Amador-Valenzuela [3], Salvatore Calabrese [1], Francesco Cappuzzello [1,4], Manuela Cavallaro [1], Suna Firat [5], Maria Fisichella [1], Alessandro Spatafora [1,4], Luis Acosta [6,7], Clementina Agodi [1], Ismail Boztosun [5], Giuseppe A. Brischetto [1,4], Daniela Calvo [8], Efrain R. Chávez Lomelí [6], Irene Ciraldo [1,4], Mauro Cutuli [1,4], Franck Delaunay [8,9,10], Nikit Deshmukh [11], Paolo Finocchiaro [1], Antonino Foti [7], Aylin Hacisalihoglu [12], Felice Iazzi [8,9], Laura La Fauci [1,4], Gaetano Lanzalone [1,13], Nilberto H. Medina [14], Djalma Mendes [2], José R. B. Oliveira [14], Athina Pakou [15], Luciano Pandola [1], Horia Petrascu [16], Federico Pinna [8,9], Giuseppe Russo [4,7], Onoufrios Sgouros [1], Selçuk O. Solakci [5], Vasilis Soukeras [1], George Souliotis [17], Domenico Torresi [1], Salvatore Tudisco [1], Aydin Yildirim [5] and Vinicius A. B. Zagatto [2]

[1] Istituto Nazionale di Fisica Nucleare, Laboratori Nazionali del Sud, 95125 Catania, Italy; calabrese@lns.infn.it (S.C.); cappuzzello@lns.infn.it (F.C.); manuela.cavallaro@lns.infn.it (M.C.); fisichella@lns.infn.it (M.F.); spatafora@lns.infn.it (A.S.); agodi@lns.infn.it (C.A.); brischetto@lns.infn.it (G.A.B.); ciraldo@lns.infn.it (I.C.); mauro.cutuli93@gmail.com (M.C.); finocchiaro@lns.infn.it (P.F.); lauralafauci1985@hotmail.it (L.L.F.); gaetano.lanzalone@unikore.it (G.L.); pandola@lns.infn.it (L.P.); sgouros@lns.infn.it (O.S.); soukeras@lns.infn.it (V.S.); torresi@lns.infn.it (D.T.); tudisco@lns.infn.it (S.T.)

[2] Instituto de Física, Universidade Federal Fluminense, Niterói 24210-340, Brazil; rlinares@id.uff.br (R.L.); dmendes@if.uff.br (D.M.); vzagatto@id.uff.br (V.A.B.Z.)

[3] Departamento de Aceleradores y Estudio de Materiales, Instituto Nacional de Investigaciones Nucleares, Ocoyoacac 52750, Mexico; paulina.amador@inim.gob.mx

[4] Dipartimento di Fisica e Astronomia "Ettore Majorana", Università di Catania, 95125 Catania, Italy; giuseppe.russo@ct.infn.it

[5] Department of Physics, Akdeniz University, Antalya 07058, Turkey; sunafirat.nuba@gmail.com (S.F.); boztosun@akdeniz.edu.tr (I.B.); oktaysolakci@akdeniz.edu.tr (S.O.S.); aydinyildirim@akdeniz.edu.tr (A.Y.)

[6] Instituto de Fisica, Universidad Nacional Autónoma de México, Mexico City 04510, Mexico; acosta@fisica.unam.mx (L.A.); chavez@fisica.unam.mx (E.R.C.L.)

[7] INFN, Sezione di Catania, 95123 Catania, Italy; a.foti@ct.infn.it

[8] INFN, Sezione di Torino, 10124 Torino, Italy; calvo@to.infn.it (D.C.); delaunay@lpccaen.in2p3.fr (F.D.); felice.iazzi@polito.it (F.I.); fpinna@to.infn.it (F.P.)

[9] DISAT, Politecnico di Torino, 10129 Torino, Italy

[10] Laboratoire de Physique Corpuscolaire de Caen, Normandie Université, Ensicaen, Unicaen, CNRS/INP3, 14000 Caen, France

[11] School of Sciences, Auro University, Surat 395007, India; nikitdeshmukh@gmail.com

[12] Institute of Natural Sciences, Karadeniz Teknik Universitesi, Trabzon 61080, Turkey; aylinayikoglu@gmail.com

[13] Facoltà di Ingegneria e Architettura, Università di Enna "Kore", 94100 Enna, Italy

[14] Instituto de Fisica, Universidade de São Paulo, São Paulo 05508-060, Brazil; medina@if.usp.br (N.H.M.); zero@if.usp.br (J.R.B.O.)

[15] Department of Physics, University of Ioannina and Hellenic Institute of Nuclear Physics, 45110 Ioannina, Greece; apakou@uoi.gr

[16] IFIN-HH, 077125 Bucarest, Romania; hpetr@nipne.ro

[17] Department of Chemistry, University of Athens and Hellenic Institute of Nuclear Physics, 15771 Athens, Greece; soulioti@chem.uoa.gr

* Correspondence: carboned@lns.infn.it

Abstract: Double charge exchange (DCE) reactions could provide experimentally driven information about nuclear matrix elements of interest in the context of neutrinoless double-β decay. To achieve this goal, a detailed description of the reaction mechanism is mandatory. This requires the full characterization of the initial and final-state interactions, which are poorly known for many of the projectile-target systems involved in future DCE studies. Among these, we intend to study the ^{20}Ne +

^{130}Te and ^{18}O + ^{116}Sn systems at 15.3 AMeV, which are particularly relevant due to their connection with the ^{130}Te→^{130}Xe and ^{116}Cd→^{116}Sn double-β decays. We measure the elastic and inelastic scattering cross-section angular distributions and compare them with theoretical calculations performed in the optical model, one-step distorted wave Born approximation, and coupled-channel approaches using the São Paulo double-folding optical potential. A good description of the experimental data in the whole explored range of transferred momenta is obtained provided that couplings with the 2_1^+ states of the projectile and target are explicitly included within the coupled-channel approach. These results are relevant also in the analysis of other quasi-elastic reaction channels in these systems, in which the same couplings should be included.

Keywords: initial state interaction; elastic and inelastic scattering; MAGNEX magnetic spectrometer; coupled-channel calculations; optical potential; double charge exchange reactions; double beta decay

1. Introduction

The intrinsic nature of neutrinos is one of major hot cases in fundamental physics. So far, it is unclear whether neutrinos are Dirac or Majorana particles. The clear-cut is the relationship between particle and its own anti-particle. In Dirac's description, elementary neutral fermionic particles and anti-particles are distinctive entities, whereas Majorana indicates that they are the same entity. The hypothesis of the symmetry between particle and anti-particle was presented by Ettore Majorana [1] in a period when neutrinos were also hypothetical particles. Later, the lepton-number conservation, observed in many decays and reactions, placed Majorana's neutrino theory aside for many decades. The discovery of neutrino oscillations brought the topic back to the debate of the scientific community and has been driving theoretical and experimental efforts. Promising experiments to establish the Majorana or Dirac nature of neutrinos are presently conceived of by searching for the neutrinoless double beta ($0\nu\beta\beta$) decay in nuclei such as ^{48}Ca, ^{76}Ge, ^{116}Cd and ^{130}Te, ^{136}Xe, with half-lives higher than 10^{25}y [2–4]. The observation of the $0\nu\beta\beta$ decay would prove the Majorana nature of neutrinos, and the measurement of the half-life would allow for the determination of the effective neutrino mass, once appropriate nuclear matrix elements (NMEs) are accurately known [5–7].

The nuclear physics community is considering the possibility of extracting data-driven information on $0\nu\beta\beta$ NME from the study of double charge exchange (DCE) reaction cross-sections induced by heavy projectiles. The main purpose of the NUMEN and NURE projects at the INFN-LNS [8–11] is to provide relevant information on the NME associated with hot cases for the $0\nu\beta\beta$ decays, by exploring the DCE reactions induced by heavy ions [12]. Other studies at RIKEN [13] and RCNP [14,15] have recently explored DCE reactions in connection to $0\nu\beta\beta$ and also to populate exotic structures. The NUMEN experimental activity includes measurements of the DCE cross-sections associated with the $0^+ \rightarrow 0^+$ transition and detection of ejectiles around $0°$ at distinct bombarding energies. Furthermore, it is mandatory to assess the contributions of possible competing mechanisms such as two-sequential single charge exchange (SCE) reactions and successive multi-nucleon transfers that lead to the same final state. Direct measurements of all steps of these competing reactions are not feasible because most scenarios involve radioactive nuclei. The approach is to measure cross-sections of some steps [16,17] and to fill the gaps by reliable direct reaction calculations.

The development of a consistent microscopic theoretical description of the DCE is essential both for the reaction mechanism and the nuclear structure sides. In the theoretical description of nuclear reactions, the role of the initial-state (ISI) and final-state (FSI) interactions is fundamental for the study of all the reaction channels. They represent the main component of the interacting nuclear potential and give the strongest contribution to the total reaction cross-section. On the contrary, the DCE processes are described as a second order perturbation of the interacting potential. The state-of-the-art reaction theory for DCE

and SCE reactions was recently developed within the NUMEN collaboration [18–22]. The distorted wave Born approximation (DWBA) amplitude for the SCE and DCE reactions can be expressed in terms of $M_{\alpha\beta} = \langle \chi_\beta^{(-)}, bB|\hat{V}|\chi_\alpha^{(+)}, aA \rangle$, where $\hat{V}$ represents the proper interaction, defined in [18,21] for the SCE and DCE, respectively. The $\chi_{\alpha\beta}^{(\pm)}$ symbols denote the incoming and outgoing distorted waves, respectively. The ISI and FSI are responsible for the distortion of the wave functions of the interacting nuclei. Thus, for the purposes of the NUMEN project, a detailed microscopic description of the DCE and SCE reaction mechanisms requires a careful determination of the ISI and FSI for the reactions of interest. These involve ^{18}O and ^{20}Ne beams at energies from 15 to 60 AMeV and the target nuclei candidate for the $0\nu\beta\beta$ decay.

Initial- and final-state ion-ion interactions for DWBA calculations of nuclear reactions can be described by optical potentials (OPs), i.e., by local potentials depending only on the relative coordinate between the colliding nuclei. Elastic and inelastic scattering are the main tools for probing the OPs [23–25]. This is usually performed from the analysis of the cross-section angular distributions by fitting the parameters of a complex Woods–Saxon potential within the optical model (OM) calculation. However, this procedure may lead to ambiguities, with different sets of parameters that reproduce the same experimental data equally well [26]. Moreover, such an approach is not suitable when the elastic channel is not experimentally measurable, e.g., for the core-core potentials involved in the multi-nucleon transfer reactions [16]. Alternatively, double-folding OPs are often considered, which fold the frozen densities of the colliding nuclei with a realistic nucleon-nucleon interaction, adopting adjustable normalization factors for the real and imaginary parts.

The presence of a nuclear rainbow structure in the angular distribution of the elastic scattering allows for accurate determination of the OPs. However, a rainbow-like structure appears in α-like systems (^{12}C + ^{16}O at 330 MeV, for example [27]) or in deformed target nuclei (^{16}O + ^{27}Al at 100 MeV and 280 MeV [28–31]) at large scattering angles and, consequently, very low cross-sections. The performance of the OPs can be better evaluated comparing the predictions for non-elastic channels, like inelastic scattering and transfer reactions with experimental data, if available. This can be accurately done by comparing the results of calculations based on the one-step distorted wave Born approximation (DWBA) and the coupled-channels (CCs) methods. In the latter approach, the relevant internal states of the projectile/target systems are explicitly taken into account, and the role of such states in the distorted wave functions of the incoming and outgoing partitions is clarified. The couplings with some inelastic scattering or reaction channels are the other main ingredients that constitute the ISI and FSI.

The present work is part of the NUMEN experimental campaign carried out with ^{20}Ne and ^{18}O beams performed at the INFN-LNS at 15.3 AMeV incident energy. Among these, the ^{20}Ne + ^{76}Ge [32], ^{20}Ne + ^{116}Cd [16,33,34], ^{18}O + ^{76}Se [35], and ^{18}O + ^{40}Ca [17,36] systems were recently studied. Optical model and coupled-channel calculations are performed to describe the experimental cross-section angular distributions extracted for the elastic and some inelastic transitions. The results obtained using different optical potentials are compared to the data, and a good agreement is reached when the São Paulo double-folding OP [37] is adopted. A relevant conclusion of these studies is that an accurate description of the experimental data requires the inclusion of couplings with the low-lying excited states. In particular, the relevant couplings have the 2_1^+ states of the projectile and target and sometimes, as for example in the ^{18}O + ^{40}Ca case [36], also with the 3_1^-.

Here, we discuss new data for the elastic and inelastic scattering of the ^{20}Ne + ^{130}Te and ^{18}O + ^{116}Sn systems in the same theoretical framework of our previous works [32,34–36]. Both target nuclei are involved in present $0\nu\beta\beta$ research. In particular, the ^{130}Te nucleus is a candidate for the $0\nu\beta\beta$ decay [38], and ^{116}Sn is the daughter nucleus for the $\beta\beta$ decay of the ^{116}Cd one [39,40]. As far as we know, no experimental measurements exist at $\approx$ 15 AMeV incident energy, and no theoretical analyses are present in the literature regarding the case of the ^{20}Ne + ^{130}Te system, although some works are focused on elastic scattering with the ^{20}Ne beam [41,42] or the ^{130}Te target [43,44]. Regard-

ing the ^{18}O + ^{116}Sn case, such analyses were performed using lighter projectiles [45] or by fitting procedures with free-parameter Woods–Saxon potentials [46], not useful for the purposes of NUMEN [8].

This paper is organized as follows: the experimental setup and the data reduction technique are described in Section 2; the theoretical framework is presented in Section 3; the obtained results are discussed in Section 4; and the conclusions are given in Section 5.

2. Experimental Setup and Results

The experiments were performed in Catania (Italy), at the INFN-LNS, using the ^{20}Ne and ^{18}O beams accelerated at 15.3 AMeV by the K800 Superconducting Cyclotron [47]. In both cases, ions were fully stripped by crossing a thin carbon foil placed along the beam line. The ^{20}Ne beam impinged on a 250 ± 10 μg/cm^2 ^{130}Te (99.75% enriched) evaporated on a 42 ± 2 μg/cm^2 carbon backing. A 950 ± 50 μg/cm^2 CH$_2$ target was placed after the primary one in order to reduce the amount of partially stripped ejectiles emerging from the target [48], which represents a background for other reaction channels measured in the same experimental campaign [8]. The ^{18}O beam impinged on a 380 ± 20 μg/cm^2 ^{116}Sn target (98% enriched), evaporated onto a thin polyvinyl formal resin backing (4.0 μg/cm^2 thick). The total beam charge was collected by a copper Faraday cup with a 0.8 cm entrance diameter and a 3 cm depth, mounted 15 cm downstream of the target. The accuracy in the charge collection was better than 10%, guaranteed by an electron suppressor polarized at -200 V and a low noise charge integrator circuit.

The ^{20}Ne and ^{18}O ejectile momenta were analyzed by the MAGNEX spectrometer [49,50] in separate runs. For the ^{20}Ne + ^{130}Te system, the spectrometer optical axis was placed at θ_{lab} = 8°, 13°, and 20° in the laboratory frame, and in the ^{18}O + ^{116}Sn system, MAGNEX was placed at θ_{lab} = 10° and 15°. The measurements were performed with the spectrometer working in full acceptance mode ($\Omega \approx 50$ msr). The measured angular range was $3° < \theta_{lab} < 26°$ and $5° < \theta_{lab} < 21°$ in the laboratory reference frame for ^{20}Ne + ^{130}Te and ^{18}O + ^{116}Sn, respectively.

For the ^{20}Ne + ^{130}Te system, a supplemental run at θ_{lab} = 8° with a reduced solid angle acceptance ($\Omega \approx 34$ msr), which intentionally excluded the most forward angles, was performed in order to get a reasonable measurement from the Faraday cup. Indeed, due to the very large cross-section at forward angles and the maximum tolerable rate by the MAGNEX focal plane detector [51,52], the beam current for the run at θ_{lab} = 8° in the full acceptance condition was limited to about 100 epA, corresponding to an unacceptable signal-to-noise ratio in the measurement of the total beam charge.

The details of the particle identification and the data reduction techniques are explained in [33,53–55]. A fully differential algebraic method [56] was implemented to perform the trajectory reconstruction technique, in which the measured horizontal and vertical positions and angles at the focal plane were required as the input. Examples of the obtained energy spectra for the $^{130}Te(^{20}Ne,^{20}Ne)^{130}Te$ and $^{116}Sn(^{18}O,^{18}O)^{116}Sn$ scattering are shown in Figure 1 in which E$_x$ = Q$_0$ - Q, where Q$_0$ is the ground-state-to-ground-state Q-value (Q$_0$ = 0 for elastic scattering). The multiple-fit procedure plotted in Figure 1 was performed to describe the energy spectra. The width of each peak was fixed according to the experimental energy resolution, including the recoil energy broadening due to the in-flight decay of the ejectile for the transitions in which it was found in a bound excited state.

In the case of $^{130}Te(^{20}Ne,^{20}Ne)^{130}Te$ scattering (Figure 1a), the obtained energy resolution of ≈ 1 MeV full width at half-maximum (FWHM) is not enough to isolate the transition to the first excited state of ^{130}Te at 0.839 MeV. A second peak is visible in the spectrum at $\approx$ 1.6 MeV, corresponding to the population of the $^{20}Ne_{1.633}(2^+)$ + $^{130}Te_{g.s.}(0^+)$, $^{20}Ne_{g.s.}(0^+)$ + $^{130}Te_{1.632}(4^+)$, and other transitions. A third peak is also visible at ≈ 2.5 MeV. In this energy region, we expect the contribution of the $^{130}Te_{0.839}(2^+)$ + $^{20}Ne_{1.633}(2^+)$ transition, among many others. The energy resolution obtained in the $^{116}Sn(^{18}O,^{18}O)^{116}Sn$ spectrum (Figure 1b) is ≈ 850 keV FWHM. It was possible to isolate the elastic transition from a second peak, corresponding to the population of the following unresolved transitions:

$^{18}\text{O}_{g.s.}(0^+) + ^{116}\text{Sn}_{1.293}(2^+)$, $^{18}\text{O}_{1.982}(2^+) + ^{116}\text{Sn}_{g.s.}(0^+)$, and a peak at ≈ 2.15 MeV corresponding to the superposition of some ^{116}Sn excited states.
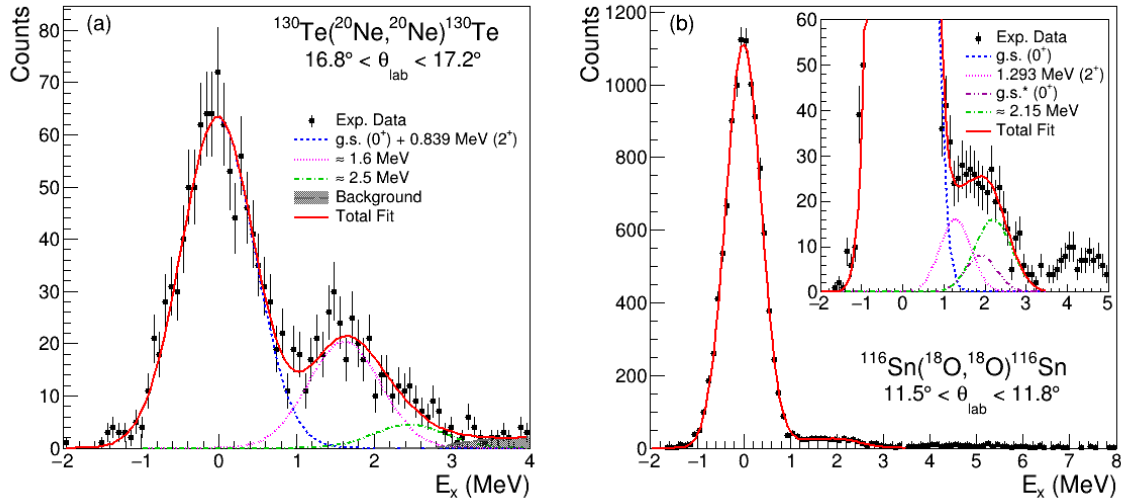

Figure 1. (**a**) Excitation energy spectrum for the $^{130}\text{Te}(^{20}\text{Ne},^{20}\text{Ne})^{130}\text{Te}$ scattering at 306 MeV incident energy and $16.8° < \theta_{lab} < 17.2°$. Lines, obtained from best-fit procedures, identify peaks corresponding to the superposition of the projectile and target states, as labeled in the legend, and the background curve represents the high level density above ≈ 3 MeV. (**b**) Excitation energy spectrum for the $^{116}\text{Sn}(^{18}\text{O},^{18}\text{O})^{116}\text{Sn}$ scattering at 275 MeV incident energy and $11.5° < \theta_{lab} < 11.8°$. Inset: Zoomed view of the low-lying excited states. Some peaks are identified in the spectrum by Gaussian fits as labeled in the legend. The dot-dot-dashed purple curve marked by an asterisk corresponds to ^{18}O in the 2_1^+ excited state at 1.982 MeV.

The absolute cross-sections were extracted following the procedures discussed in [55], taking into consideration the overall MAGNEX efficiency [57]. The experimental cross-section angular distributions extracted for the quasi-elastic (elastic + 2_1^+ at 0.839 MeV) in the $^{20}\text{Ne} + ^{130}\text{Te}$ system, elastic in the $^{18}\text{O} + ^{116}\text{Sn}$ one, and some inelastic transitions are shown in Figures 2–5. The corresponding scale of transferred linear momentum q is also given. The error bars include uncertainties coming from the statistical contribution, solid angle estimation, and fitting procedure.

The elastic scattering data shown in Figure 2b for the $^{18}\text{O} + ^{116}\text{Sn}$ system are in good agreement with the Rutherford cross-section at very forward angles, without the need for any scaling factor, whereas in the $^{130}\text{Te}(^{20}\text{Ne},^{20}\text{Ne})^{130}\text{Te}$ scattering (Figure 2a), a scale factor equal to 1.5 was applied to all the experimental points to ensure the same agreement. This value is larger than the systematic errors coming from the target thickness and the total charge collected by the Faraday cup ($\approx 10\%$). This was associated with efficiency losses in the focal plane detector induced by the high counting rate, not recoverable using the standard procedure [57].

The quasi-elastic and elastic scattering cross-sections expressed in terms of the ratio to the Rutherford one are shown in Figures 3 and 5a, respectively. The scattering is dominated by the Coulomb field up to the grazing angle (θ_{gr}), located at $\theta_{gr} \approx 16°$ and $\theta_{gr} \approx 14°$ in the center-of-mass (c.m.) reference frame for the $^{20}\text{Ne} + ^{130}\text{Te}$ and $^{18}\text{O} + ^{116}\text{Sn}$ systems, respectively. Beyond θ_{gr}, the distributions show the characteristic fall-off associated with the near-side scattering amplitudes, since in that region, the data are more responsive to the nuclear part of the nucleus-nucleus potential. Differential cross-section angular distributions were extracted also for some inelastic transitions. In particular, Figure 4 shows the angular distributions for the $^{20}\text{Ne} + ^{130}\text{Te}$ system corresponding to the peak at ≈ 1.6 MeV (Panel a) and at ≈ 2.5 MeV (Panel b). The angular distribution for the peak at ≈ 1.9 MeV in the $^{18}\text{O} + ^{116}\text{Sn}$ spectrum (corresponding to the sum of the three Gaussian fits in Figure 1b) is shown in Figure 5b.
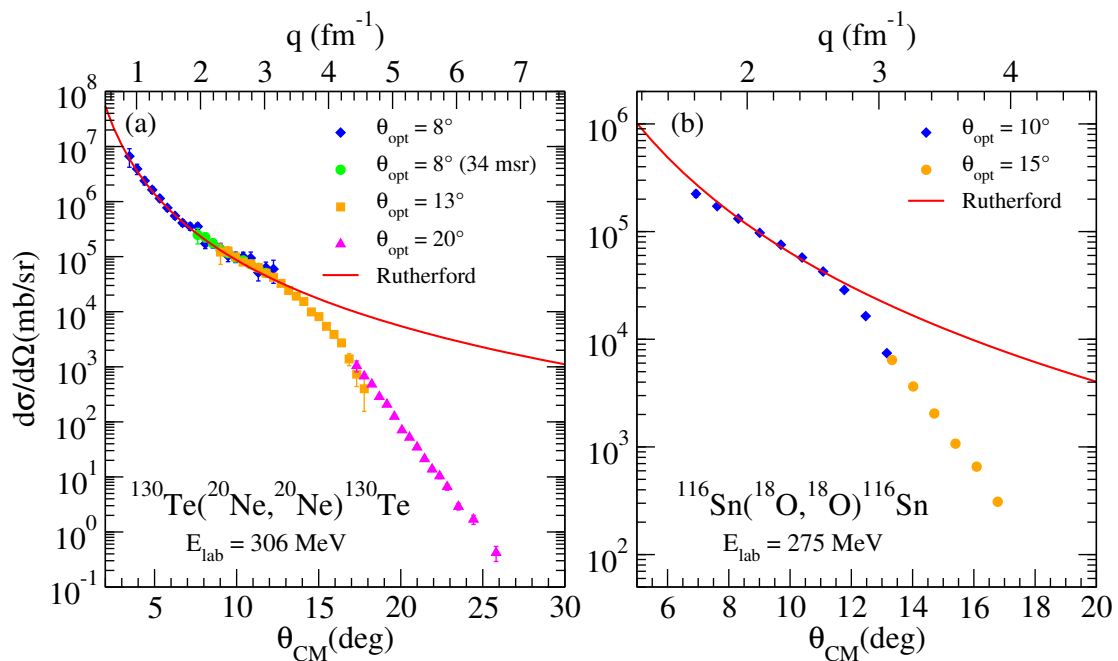
Figure 2. (**a**) Quasi-elastic cross-section angular distribution in the ^{20}Ne +^{130}Te system (see the text) and (**b**) elastic cross-section angular distribution in the ^{18}O +^{116}Sn system. Different markers correspond to data collected in separate runs for different angular settings (see the text). The red line represents the Rutherford cross-section.
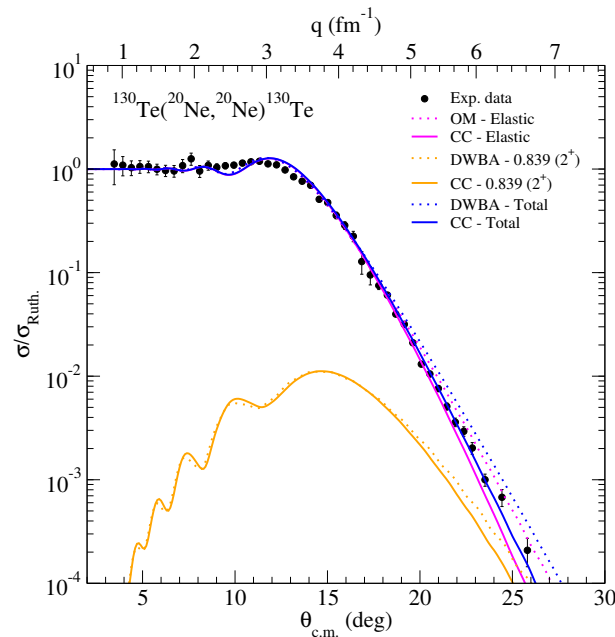
Figure 3. Cross-section angular distribution of the quasi-elastic scattering in the ^{20}Ne + ^{130}Te system at E_{lab} = 306 MeV in terms of the ratio with the Rutherford cross-section ($\sigma_{Ruth.}$). Contributions from the 2_1^+ excited state of ^{130}Te at 0.839 MeV are present (see the text). The experimental points are obtained from the ones in Figure 2a by a weighted average in the overlap region between two angular sets. Calculations for the elastic transition for the OM and CCs approaches are shown with the dotted and continuous magenta line, respectively. The contribution of the 2_1^+ state of ^{130}Te for the one-step DWBA and CCs approaches is represented by the dotted and continuous orange lines, respectively. The sum of the OM result for the elastic channel and the DWBA one for the 0.839 MeV are shown as the dotted blue lines. The sum of the two CCs' calculations is indicated by the continuous blue line.
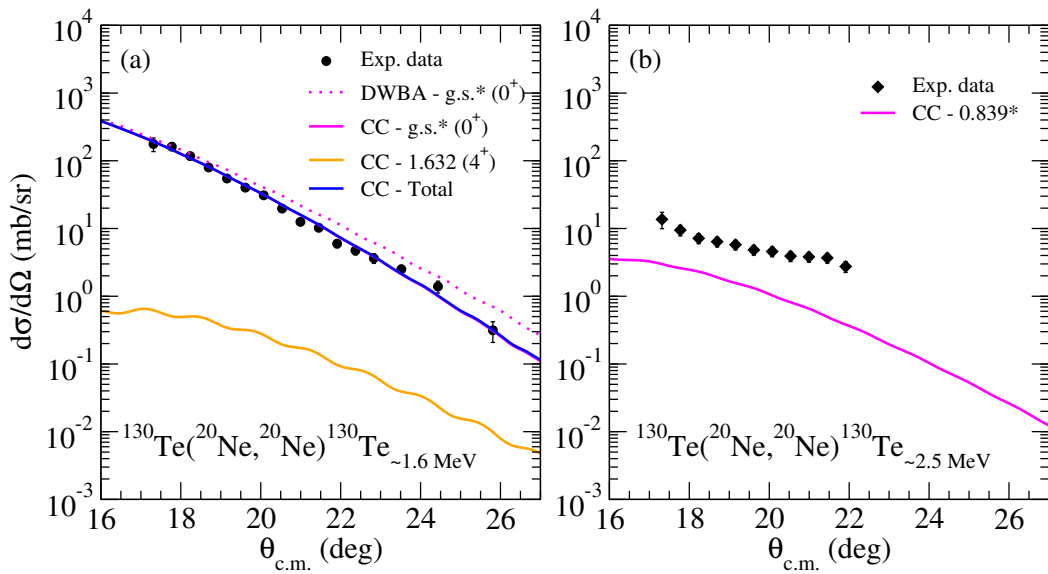
Figure 4. Inelastic cross-section angular distributions in the ^{20}Ne + ^{130}Te system at E$_{lab}$ = 306 MeV. The energies indicated in the legend refer to the ^{130}Te nucleus. The asterisks identify transitions in which the ^{20}Ne ejectile is in the 2_1^+ excited state at 1.633 MeV. (**a**) Cross-section associated with the peak at ≈ 1.6 MeV in Figure 1a. Theoretical calculations for the ^{20}Ne$_{1.633}(2^+)$ + ^{130}Te$_{g.s.}(0^+)$ transition are shown with the dotted and continuous magenta lines for the one-step DWBA and CCs approaches, respectively. The orange line represents the CCs' calculations for the 4^+ state of ^{130}Te at 1.632 MeV. The sum of the two is shown as the blue line. (**b**) Cross-section associated with the peak at ≈ 2.5 MeV in Figure 1a. The magenta line represents theoretical calculations for ^{20}Ne$_{1.633}(2^+)$ + ^{130}Te$_{0.839}(2^+)$.
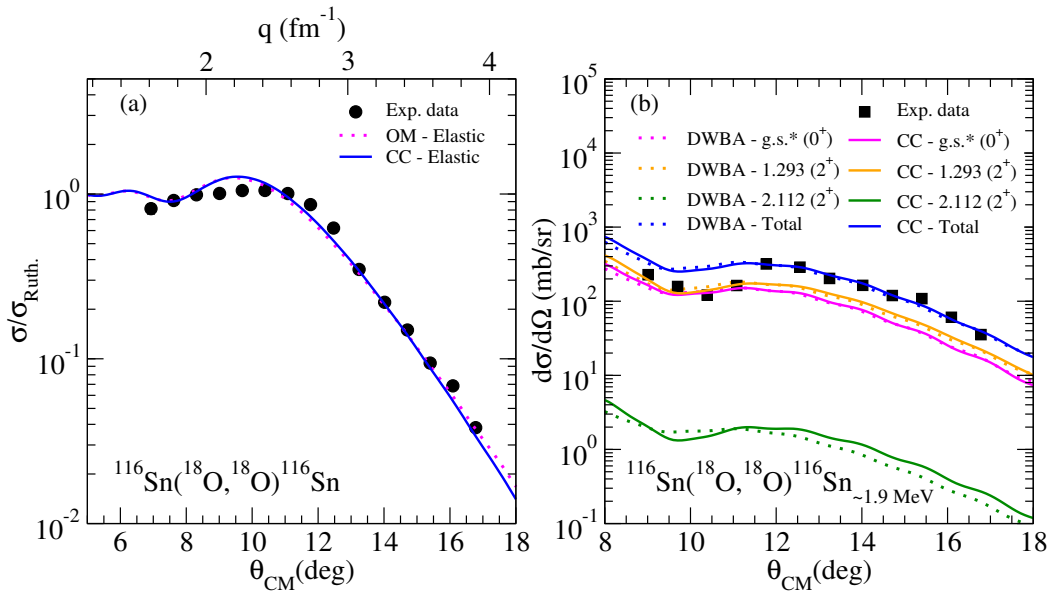
Figure 5. Cross-section angular distributions for the ^{18}O + ^{116}Sn system at E$_{lab}$ = 275 MeV. The energies indicated in the legend refer to the ^{116}Sn nucleus. The asterisks identify transitions in which the ^{18}O ejectile is in the 2_1^+ excited state at 1.982 MeV. (**a**) Elastic scattering angular distribution in terms of the ratio with the Rutherford cross-section ($\sigma_{Ruth.}$). The experimental points are obtained from those in Figure 2b by a weighted average in the overlap region between two angular sets. Theoretical calculations with the OM and CCs approaches are shown as the dotted magenta and continuous blue lines, respectively. (**b**) Inelastic cross-section angular distribution for the peak at ≈ 1.9 MeV in Figure 1b. Theoretical calculations for the ^{18}O$_{1.982}(2^+)$ + ^{116}Sn$_{g.s.}(0^+)$, ^{18}O$_{g.s.}(0^+)$ + ^{116}Sn$_{1.293}(2^+)$, and ^{18}O$_{g.s.}(0^+)$ + ^{116}Sn$_{2.112}(2^+)$ transitions are shown with magenta, orange, and green lines, respectively. The sum is indicated by the blue lines. For each transition, the one-step DWBA and CCs' calculations are reported with the dotted and continuous lines, respectively.

3. Theoretical Analysis

The data were compared with theoretical calculations performed in the OM, one-step DWBA, and CCs approaches using the FRESCO code [58]. The double-folding São Paulo potential (SPP) [37] was adopted as the bare potential ($V_{\mathrm{SPP}}(R)$) of the OP,

$$V_{\mathrm{nuc.}}(R) = (N_r + iN_i)V_{\mathrm{SPP}}(R), \qquad (1)$$

with real and imaginary strength factors N_r and N_i, respectively. The double-folding $V_{\mathrm{SPP}}(R)$ is calculated using two-parameter Fermi distributions for the matter densities with radius and diffuseness parameters obtained from a systematic analysis of electron scattering data and mean field calculations based on the Hartree–Fock–Bogoliubov theory [37]. In particular, the average matter density diffuseness (a_m) is 0.56 fm, although small variations are allowed to accommodate nuclear structure effects that mostly present at the surface. In particular, in the ^{18}O projectile, to account for the effect generated by the two valence neutrons bounded to the ^{16}O core, we adopted a larger $a_m = 0.61$ fm, as typically done [35,36,59–61].

In the OM framework, the one-channel scattering equation is solved, and the OP accounts for the average effect from other reaction channels. In a step further, the one-step DWBA solves sets of two equations, consisting of an elastic and an another channel. These channels are connected by a coupling potential, although back coupling effects are not considered. Consequently, the elastic cross-section within this approach does not deviate from the one obtained from the simple one-channel calculation. This is a reasonable approach whenever the coupling potential is weak. Finally, the CC considers the full coupling scheme, consisting of elastic and inelastic channels. This also includes back coupling effects, not present in the one-step DWBA. Therefore, comparison between the results from one-step DWBA and CCs tells about the importance of coupling potentials on the elastic channel.

OM calculations, using the SPP defined in Equation (1) with $N_r = 1.0$ and $N_i = 0.78$, describe the elastic scattering data of many systems [62]. This set of parameters was used also in the OM and one-step DWBA calculations presented here. In the CCs' calculations we adopted a smaller factor, $N_i = 0.6$, since, in such cases, we are explicitly including the effect of some non-elastic channels in the elastic cross-sections. The imaginary part of the OP effectively takes into account the loss of flux to dissipative processes such as deep inelastic collisions. Within the CC and coupled reaction channel calculations, this value has been shown to describe reasonably well the data for elastic and inelastic scattering in ^{16}O + ^{27}Al [29,30] and ^{16}O + ^{60}Ni [31] at energies above the Coulomb barrier.

The coupling potentials are key ingredients in such calculations and, in macroscopic models, are usually written in terms of multipole decomposition [24]. For Coulomb excitation, each λ-component depends on the corresponding reduced matrix element for the electric operator, which is connected with the reduced transition probability $B(E\lambda \uparrow)$. Nuclear excitations are usually considered as a deformation of the charge or matter distribution of the nucleus. Deformation of the nuclear surface is decomposed into spherical harmonic terms with respect to a spherical shape. The nuclear coupling potentials are determined as:

$$F_\lambda(R) = -\delta_\lambda^{\mathrm{m}} \frac{1}{\sqrt{4\pi}} \frac{dV_{\mathrm{nuc.}}(R)}{dR}, \qquad (2)$$

where $\delta_\lambda^{\mathrm{m}}$ is the matter deformation length of the λ-pole component.

Following Khoa and Satchler, the precedent method is referred to as the deformed optical potential [63]. Usually, it is assumed that the optical potential is independent of the channel state and deformed in the same way as the density distribution of the excited nuclei (equal deformation hypothesis). $\delta_\lambda^{\mathrm{m}}$ is often assumed to be equal for charge and mass distributions. Therefore, the matter deformation length is associated with the charge

distribution and determined from the electric reduced transition probability from state I^π to $I'^{\pi'}$, $B(E\lambda; I \to I')$:

$$\delta_\lambda = \frac{4\pi}{3ZR^{\lambda-1}}\sqrt{(2I+1)B(E\lambda; I \to I')/e^\lambda}. \tag{3}$$

where $R = 1.2A^{1/3}$ is the nuclear radius. This expression assumes that Z protons are uniformly distributed in a sphere with radius R (the so-called sharp cut-off model), which can be replaced by a more realistic distribution with a finite diffuseness [64].

The equal deformation hypothesis for matter distribution and potential is, in fact, correct if the projectile is a point-like particle and the potential is obtained by folding the density with a zero-range interaction (see Chap. 14 in [24]). For heavy nuclear systems, we adopted a deformation length corrected for the deformed potential to take into account the relative differences in the density and potential radii, as follows:

$$\delta_\lambda^{\text{corr.}} = \frac{R}{R_{\text{pot.}}}\delta_\lambda, \tag{4}$$

where $R_{\text{pot.}}$ is the radius of the optical potential, listed in Table 1 for the two systems together with the volume integrals. The results agree with the typical values [24], confirming a reasonable description of the optical potential properties. In addition, the deformation of the imaginary part is also considered. This is justified as an effective procedure to account for possible couplings of the considered channels to collective states not explicitly included in the coupling scheme [31]. We assume that the imaginary deformation length is equal to the matter deformation ($\delta_\lambda^{\text{Im.}} \equiv \delta_\lambda^{\text{corr.}}$).
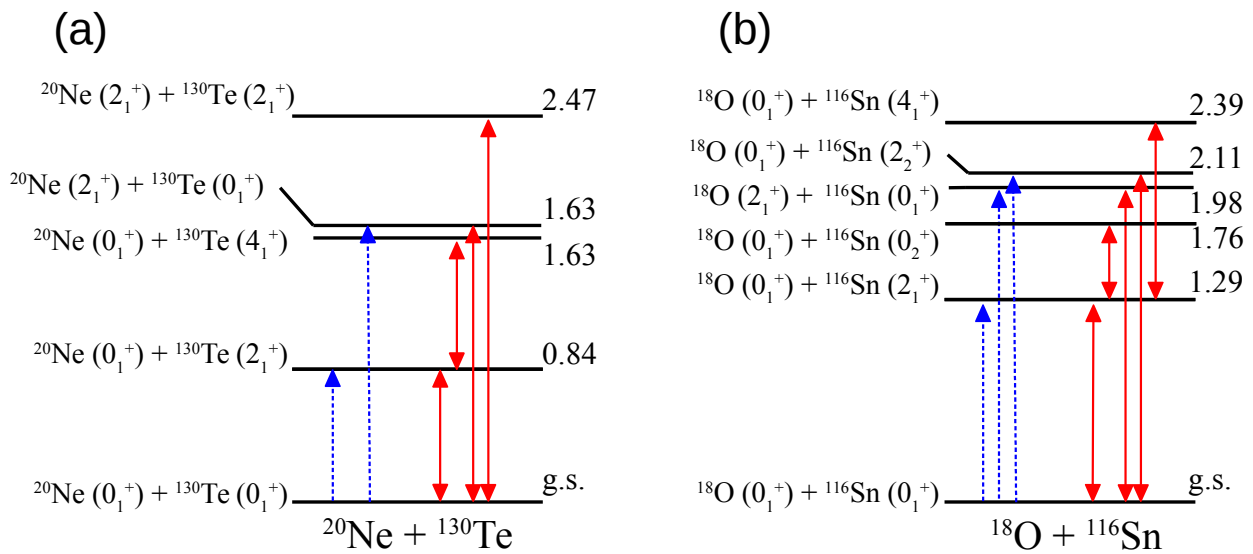
Table 1. Radii of the São Paulo potential (SPP) potential $R_{pot.}$ and volume integrals J per interacting pair for the real (V) and the imaginary (W) parts within the one-step distorted wave Born approximation (DWBA) ($N_i = 0.78$) and coupled-channels (CCs) ($N_i = 0.6$) approaches.

System	$R_{\text{pot.}}$ (fm)	J_V (MeV fm³)	J_W^{DWBA} (MeV fm³)	J_W^{CC} (MeV fm³)
^{20}Ne+^{130}Te	5.66	-339.6	-264.9	-203.8
^{18}O+^{116}Sn	5.45	-339.8	-265.0	-203.9

The couplings considered in this work are sketched in Figure 6, Panel (a) for ^{20}Ne + ^{130}Te and (b) for ^{18}O + ^{116}Sn. The dotted blue and continuous red arrows indicate couplings within the one-step DWBA and CCs' calculations, respectively. The reduced transition probabilities considered for these couplings are listed in Table 2.

Table 2. Reduced transition probabilities $B(E\lambda; I \to I')$ adopted in this work. The $\delta_2^{corr.}$ is calculated using Equation (4) with the radius of the matter distribution (R) and the radius of the double-folding optical potential (see Table 1).

Nuclei	Transition $(I^\pi \to I'^{\pi'})$	Initial State (MeV)	Final State (MeV)	$B(E\lambda; I \to I')$ (e^2b^2)	$\delta_2^{\text{corr.}}$ (fm)	Ref.
^{18}O	$0^+ \to 2^+$	0.00	1.98	0.0043	0.63	[65]
^{20}Ne	$0^+ \to 2^+$	0.00	1.63	0.034	1.35	[66]
^{116}Sn	$0^+ \to 2^+$	0.00	1.29	0.209	0.70	[66]
^{116}Sn	$0^+ \to 2^+$	0.00	2.11	0.0021	0.07	[67]
^{116}Sn	$2^+ \to 0^+$	1.29	1.76	0.060	0.84	[68]
^{116}Sn	$2^+ \to 4^+$	1.29	2.39	0.076	0.95	[67]
^{130}Te	$0^+ \to 2^+$	0.00	0.84	0.295	0.77	[66]
^{130}Te	$2^+ \to 4^+$	0.84	1.63	0.059	0.35	[66]

(a)

^{20}Ne (2_1^+) + ^{130}Te (2_1^+) ──────────── 2.47

^{20}Ne (2_1^+) + ^{130}Te (0_1^+) ──────── 1.63

^{20}Ne (0_1^+) + ^{130}Te (4_1^+) ──────── 1.63

^{20}Ne (0_1^+) + ^{130}Te (2_1^+) ──────── 0.84

^{20}Ne (0_1^+) + ^{130}Te (0_1^+) ──────── g.s.

^{20}Ne + ^{130}Te

(b)

^{18}O (0_1^+) + ^{116}Sn (4_1^+) ──────── 2.39

^{18}O (0_1^+) + ^{116}Sn (2_2^+) ──────── 2.11

^{18}O (2_1^+) + ^{116}Sn (0_1^+) ──────── 1.98

^{18}O (0_1^+) + ^{116}Sn (0_2^+) ──────── 1.76

^{18}O (0_1^+) + ^{116}Sn (2_1^+) ──────── 1.29

^{18}O (0_1^+) + ^{116}Sn (0_1^+) ──────── g.s.

^{18}O + ^{116}Sn

Figure 6. Coupling scheme for the (**a**) ^{20}Ne+^{130}Te and (**b**) ^{18}O+^{116}Sn systems considered in this work. Couplings considered in the one-step DWBA and CCs' calculations are indicated by the dotted blue and red continuous arrows, respectively. Values on the right are the corresponding excitation energies (in MeV).

4. Discussion

4.1. The ^{20}Ne+^{130}Te System

The results of the OM, one-step DWBA, and CCs' calculations for the quasi-elastic and inelastic scattering in ^{20}Ne + ^{130}Te are shown in Figures 3 and 4, respectively. In the quasi-elastic scattering, we expect contributions to the cross-section from the 2_1^+ excited state of ^{130}Te at 0.839 MeV, which is not separated from the elastic peak due to the energy resolution (see Figure 1a). The results of the theoretical calculations are compared to the scattering data in Figure 3. The elastic channel is calculated within the OM and CC formalisms. The target excitation at 0.839 MeV (2_1^+ in ^{130}Te) is considered within the one-step DWBA and CCs approaches. According to the calculations, its contribution starts to be relevant compared to the elastic cross-section at larger angles ($\theta_{c.m.} \geq 20°$). Looking at the sum of the two contributions in Figure 3, it appears that the agreement between the data and calculations is good provided that the couplings are fully taken into account in the CCs approach. The DWBA results, indeed, overestimate the experimental cross-section at larger angles, where the effect of couplings start to be more relevant.

The experimental cross-section angular distribution of the peak at ≈1.6 MeV in Figure 1a is compared to the calculations in Figure 4a. The states included in the CCs' calculations are those indicated by the red arrows in the coupling scheme of Figure 6a, i.e., ^{20}Ne$_{1.633}$(2^+) + ^{130}Te$_{g.s.}$(0^+) and ^{20}Ne$_{g.s.}$(0^+) + ^{130}Te$_{1.632}$(4^+). In the one-step DWBA calculations, only the 2_1^+ state in ^{20}Ne is present, since it is not possible to reach 4^+ transitions within the adopted approach. According to the calculations, the analyzed inelastic cross-section is mainly coming from the excitation of the 2_1^+ state in ^{20}Ne. Again, the good agreement between the theories and data is achieved when the full coupling effects are explicitly taken into account in the CCs approach. This result is consistent with the conclusions drawn in the ^{20}Ne + ^{76}Ge [32] and ^{20}Ne + ^{116}Cd [34], in which the CCs' analysis was necessary to reproduce the data, and the inclusion of the 2_1^+ state in ^{20}Ne gives the strongest contribution in that energy region.

For the analysis of the third peak visible in the ^{20}Ne + ^{130}Te spectrum (see Figure 1a), only the ^{20}Ne$_{1.633}$(2^+) + ^{130}Te$_{0.839}$(2^+) transition was included in the CCs' calculations. The results, shown in Figure 4b, underestimate the experimental data by a factor of ≈2. The contribution of many other excited states of ^{130}Te (about 30) is expected

in this energy region. These channels were not included in our coupling scheme due to a lack of tabulated values on the corresponding $B(E\lambda; I \to I')$. Regardless, the contribution of the simultaneous excitation of the 2_1^+ states of the projectile and target is found to give a significant contribution to the total cross-section.

4.2. The $^{18}O+^{116}Sn$ System

The results obtained for the $^{18}O + ^{116}Sn$ system are shown in Figure 5. The calculations for the elastic transition describe quite well the experimental data both with the OM and CCs approaches (see Figure 5a). In Figure 5b, the cross-section angular distribution for the peak at ≈ 1.9 MeV is shown. This peak, visible in Figure 1b, corresponds to the excitation of the 2_1^+ state of the ^{18}O ejectile at 1.982 MeV, 2_1^+ at 1.293 MeV of ^{116}Sn, and other excited states of ^{116}Sn. In the calculations, we included only the 2_1^+ states of the projectile and target and the 2_2^+ state of ^{116}Sn at 2.122 MeV, as indicated in the coupling scheme of Figure 6b. The contribution of the 2_2^+ state of ^{116}Sn is found to be negligible, since it is about two orders of magnitude lower than the data. The experimental cross-section is described quite well including the $^{18}O_{g.s.}(0^+) + ^{116}Sn_{1.293}(2^+)$ transition, which gives the largest contribution, and the $^{18}O_{1.982}(2^+) + ^{116}Sn_{g.s.}(0^+)$ one. This result confirms what we found in the $^{18}O + ^{76}Se$ [35] and $^{18}O + ^{40}Ca$ systems [36], in which the most important contribution to the cross-section was given by the 2_1^+ states of the projectile and target nuclei.

As observed for the elastic data, in the explored range of momentum transfer q, the effects of the couplings to the inelastic channels are not visible (see Figure 5b). Indeed, as seen in the $^{20}Ne + ^{130}Te$ case, such effects become evident at $q \gtrsim 5$ fm^{-1}. Experimental measurements at larger angles, thus exploring larger values of momentum transfer, would be needed for the $^{116}Sn(^{18}O,^{18}O)^{116}Sn$ scattering.

4.3. Initial State Interactions

In the previous sections, we compared the theoretical CCs' calculations performed with the SPP double-folding potential, defined in Equation (1), with $N_r = 1.0$ and $N_i = 0.6$, to the experimental data of elastic and inelastic scattering, obtaining a quite good agreement for all the cases. The obtained ISI for the two analyzed systems are shown in Figure 7. The nuclear real and imaginary parts of the SPP are shown together with the Coulomb potential as well. The Coulombic radius of the system, $R_c = 1.2(A_{target}^{1/3} + A_{projectile}^{1/3})$ fm, is indicated by the green dotted lines. The ISI determined here is a key ingredient for the description of all the other direct reaction channels involving the same projectile-target system at the same incident energy and angular momentum transfer, e.g., multi-nucleon transfer reactions, provided that it is possible to adopt the coupled-channel Born approximation (CCBA) and coupled-reaction channels (CRCs) approaches.

However, the explicit inclusion of the couplings with the relevant excited states is not feasible when more complex reaction nets need to be calculated, such as SCE or DCE reactions, where at most DWBA calculations are typically performed [18,21,22]. Following the approach of [69], it is possible to deduce an effective polarization potential that incorporates the effect of channel coupling in the elastic optical potential. In the present study, this complex polarization potential affects the nuclear potential in the vicinity of the R_c, as shown by the continuous and dot-dashed curves. The polarization potential can be added to the determined optical potentials, used to perform the CCs' calculations, to get the coupled-channel equivalent polarization potential (CCEP) [36]. The ISI corresponding to the CCEP for the two explored systems is reported in Figure 7.

The CCEP was successfully used in one-channel calculations giving a quite reasonable description of the CCs' elastic angular distribution [70]. The same approach was recently adopted for DWBA cross-section calculation of SCE reactions [36] and can be extended also to DCE.
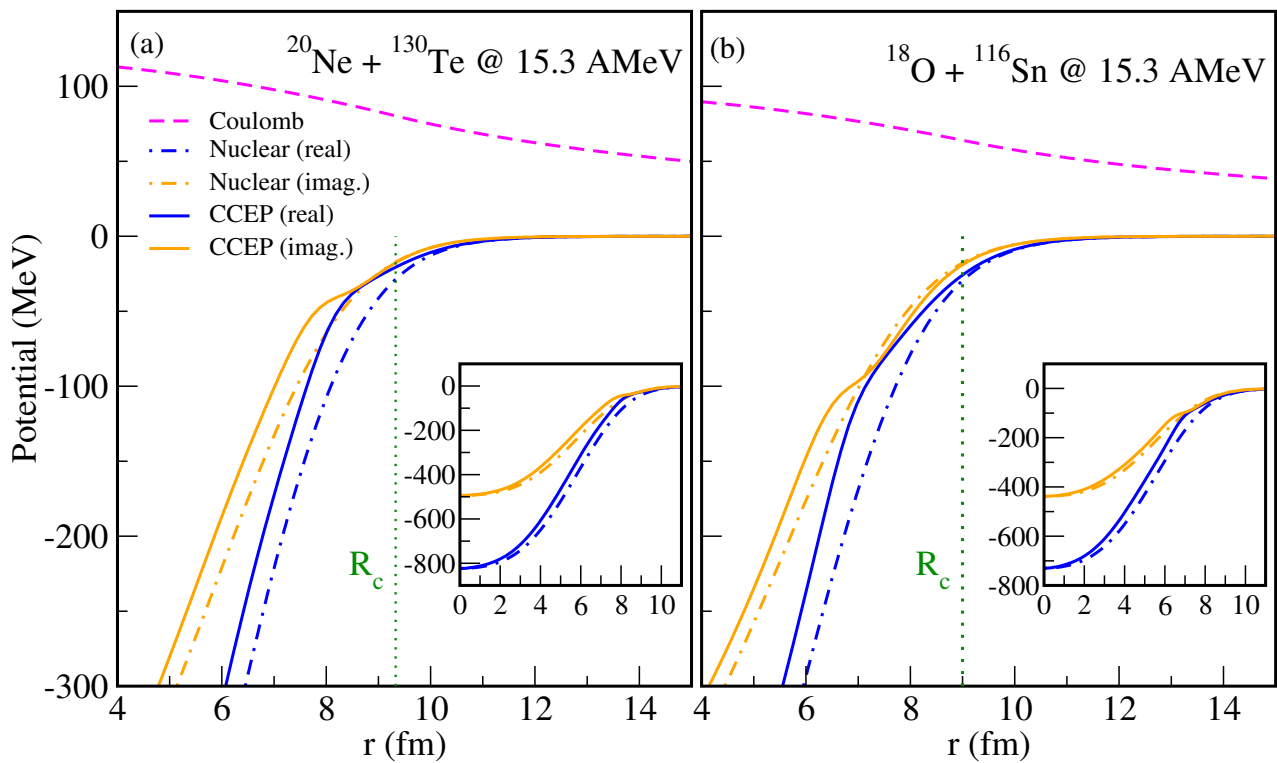
Figure 7. Initial state interactions for the (**a**) ^{20}Ne+^{130}Te and (**b**) ^{18}O+^{116}Sn systems at 15.3 AMeV considered in this work. The Coulomb potential is shown as the magenta dashed line. The nuclear real and imaginary parts of the SPP double-folding optical potential are shown as the blue and orange dashed-dotted lines, respectively. The real and imaginary parts of the coupled-channel equivalent polarization potential (CCEP), obtained from the sum of the SPP and the polarization potential, are shown as the blue and orange lines, respectively. The coulomb radius (R_c) is also indicated as the green dotted line. In the insets, the nuclear and CCEP potentials are shown in the full range of values.

5. Conclusions

This work presents new data for the quasi-elastic and inelastic scattering in the ^{20}Ne + ^{130}Te system and for the elastic and inelastic scattering in the ^{18}O + ^{116}Sn one at 15.3 AMeV measured within the NUMEN project. A wide range of transferred momenta is explored in a few angular settings, with a good agreement between independent measurements. Up to eight orders of magnitude in the cross-section are explored for the elastic scattering. The uncertainties in the experimental points are small for the whole angular range thanks to a careful tuning of the experimental setup and the advanced techniques adopted during the data reduction.

The experimental results are compared with theoretical calculations performed within the OM, one-step DWBA, and CCs approaches to assess the ISI for the two systems of interest from the NUMEN research perspective. In both cases, a satisfactory description of the elastic and inelastic data is obtained with CCs' calculations, using the São Paulo double-folding potential as the imaginary nucleus-nucleus OP, with $N_r = 1.0$ and $N_i = 0.6$, and deformation lengths corrected to account for the relative differences in the density and potential radii. In the ^{20}Ne + ^{130}Te system, we can conclude that the couplings with the 2_1^+ excited state of the projectile are important, whereas for ^{18}O + ^{116}Sn, we cannot draw the same conclusion, due to the small momentum transfer explored ($q < 4$ fm^{-1}) in the narrow range of scattering angles. These couplings are also important to determine the ISI in similar systems at similar incident energy and momentum transfer (^{20}Ne + ^{76}Ge, ^{20}Ne + ^{116}Cd, ^{18}O + ^{76}Se, and ^{18}O + ^{40}Ca).

The determination of the ISI for the ^{20}Ne + ^{130}Te and ^{18}O + ^{116}Sn systems achieved in this work is fundamental for the description of all the other quasi-elastic reaction channels induced at the same incident energy and angular momentum transfer. We derived two

different optical potentials to be used in the full net of reactions of interest for the NUMEN project. When the CCBA and CRC approaches are feasible, the SPP double-folding potential can be used with the explicit inclusion of the relevant couplings investigated here. For the more involved reaction dynamics, such as SCE and DCE reactions, the use of the DWBA approaches with the CCEP can be exploited to incorporate the couplings in an effective way.

Conflicts of Interest: The funders had no role in the design of the study; in the collection, analyses, or interpretation of data; in the writing of the manuscript; nor in the decision to publish the results.

References

1.　Majorana, E. Teoria simmetrica dell'elettrone e del positrone. *Nuovo C.* **1937**, *14*, 171–184. [CrossRef]
2.　Dell'Oro, S.; Marcocci, S.; Viel, M.; Vissani, F. Neutrinoless double beta decay: 2015 review. *Adv. High Energy Phys.* **2016**, *2016*, 2162659. [CrossRef]
3.　Dolinski, M.J.; Poon, A.W.; Rodejohann, W. Neutrinoless Double-Beta Decay: Status and Prospects. *Annu. Rev. Nucl. Part. Sci.* **2019**, *69*, 219–251. [CrossRef]
4.　Agostini, M.; Araujo, G.R.; Bakalyarov, A.M.; Balata, M.; Barabanov, I.; Baudis, L.; Bauer, C.; Bellotti, E.; Belogurov, S.; Bettini, A.; et al. Final Results of GERDA on the Search for Neutrinoless Double-β Decay. *Phys. Rev. Lett.* **2020**, *125*, 252502. [CrossRef]
5.　Ejiri, H.; Suhonen, J.; Zuber, K. Neutrino–nuclear responses for astro-neutrinos, single beta decays and double beta decays. *Phys. Rept.* **2019**, *797*, 1–102. [CrossRef]
6.　Ejiri, H. Neutrino-Mass Sensitivity and Nuclear Matrix Element for Neutrinoless Double Beta Decay. *Universe* **2020**, *6*, 225. [CrossRef]
7.　Menéndez, J. Neutrinoless $\beta\beta$ decay mediated by the exchange of light and heavy neutrinos: The role of nuclear structure correlations. *J. Phys. G Nucl. Part. Phys.* **2017**, *45*, 014003. [CrossRef]
8.　Cappuzzello, F.; Agodi, C.; Cavallaro, M.; Carbone, D.; Tudisco, S.; Lo Presti, D.; Oliveira, J.R.B.; Finocchiaro, P.; Colonna, M.; Rifuggiato, D.; et al. The NUMEN project: NUclear Matrix Elements for Neutrinoless double beta decay. *Eur. Phys. J. A* **2018**, *54*, 72. [CrossRef]
9.　Cavallaro, M.; Aciksoz, E.; Acosta, L.; Agodi, C.; Auerbach, N.; Bellone, J.; Bijker, R.; Bianco, S.; Bonanno, D.; Bongiovanni, D.; et al. NURE: An ERC project to study nuclear reactions for neutrinoless double beta decay. In Proceedings of the 55th International Winter Meeting on Nuclear Physics—PoS(BORMIO2017), Bormio, Italy, 23–27 January 2017; p. 015.
10.　Agodi, C.; Cappuzzello, F.; Cavallaro, M.; Bondì, M.; Carbone, D.; Cunsolo, A.; Foti, A. Heavy Ions Double Charge Exchange reactions: Towards the $0\nu\beta\beta$ Nuclear Matrix Element determination. *Nucl. Part. Phys. Proc.* **2015**, *265-266*, 28–30. [CrossRef]
11.　Agodi, C.; Russo, A.D.; Calabretta, L.; D'Agostino, G.; Cappuzzello, F. NUMEN project towards new experiments with high intensity beams. *Universe* submitted.

12. Cappuzzello, F.; Cavallaro, M.; Agodi, C.; Bondì, M.; Carbone, D.; Cunsolo, A.; Foti, A. Heavy-ion double charge exchange reactions: A tool toward $0\nu\beta\beta$ nuclear matrix elements. *Eur. Phys. J. A* **2015**, *51*, 145. [CrossRef]

13. Kisamori, K.; Shimoura, S.; Miya, H.; Michimasa, S.; Ota, S.; Assie, M.; Baba, H.; Baba, T.; Beaumel, D.; Dozono, M.; et al. Candidate Resonant Tetraneutron State Populated by the ^{4}He(^{8}He,^{8}Be) Reaction. *Phys. Rev. Lett.* **2016**, *116*, 052501. [CrossRef] [PubMed]

14. Matsubara, H.; Takaki, M.; Uesaka, T.; Shimoura, S.; Aoi, N.; Dozono, M.; Fujii, T.; Hatanaka, K.; Hashimoto, T.; Kawabata, T.; et al. Spectroscopic Measurement in ^{9}He and ^{12}Be. *Few Body Syst.* **2013**, *54*, 1433–1436. [CrossRef]

15. Takahisa, K.; Ejiri, H.; Akimune, H.; Fujita, H.; Matumiya, R.; Ohta, T.; Shima, T.; Tanaka, M.; Yosoi, M. Double charge exchange (^{11}B,^{11}Li) reaction for double beta decay response. *arXiv* **2017**, arXiv:1703.08264.

16. Carbone, D.; Ferreira, J.L.; Calabrese, S.; Cappuzzello, F.; Cavallaro, M.; Hacisalihoglu, A.; Lenske, H.; Lubian, J.; Agodi, C.; Borello-Lewin, T.; et al. Analysis of two-nucleon transfer reactions in the ^{20}Ne $+^{116}$Cd system at 306 MeV. *Phys. Rev. C* **2020**, *102*, 044606. [CrossRef]

17. Ferreira, J.; Carbone, D.; Cavallaro, M.; Deshmukh, N.; Agodi, C. Analysis of two-proton transfer in the ^{40}Ca(^{18}O,^{20}Ne)^{38}Ar reaction at 270 MeV incident energy. *Phys. Rev. C* accepted.

18. Lenske, H.; Bellone, J.I.; Colonna, M.; Lay, J.A. Theory of Single Charge Exchange Heavy Ion Reactions. *Phys. Rev. C* **2018**, *98*, 044620. [CrossRef]

19. Santopinto, E.; García-Tecocoatzi, H.; Magaña Vsevolodovna, R.; Ferretti, J. Heavy-ion double-charge-exchange and its relation to neutrinoless double-β decay. *Phys. Rev. C* **2018**, *98*, 061601. [CrossRef]

20. Lenske, H. Probing Double Beta-Decay by Heavy Ion Charge Exchange Reactions. *J. Phys. Conf. Ser.* **2018**, *1056*, 012030. [CrossRef]

21. Lenske, H.; Cappuzzello, F.; Cavallaro, M.; Colonna, M. Heavy ion charge exchange reactions as probes for nuclear β-decay. *Prog. Part. Nucl. Phys.* **2019**, *109*, 103716. [CrossRef]

22. Bellone, J.I.; Burrello, S.; Colonna, M.; Lay, J.A.; Lenske, H. Two-step description of heavy ion double charge exchange reactions. *Phys. Lett. B* **2020**, *807*, 135528. [CrossRef]

23. Hodgson, P.E. *Nuclear Reactions and Nuclear Structure*; Clarendon Press: Oxford, UK, 1971.

24. Satchler, G.R. *Direct Nuclear Reactions*; Oxford University Press: Oxford, UK, 1983.

25. Glendenning, N.K. *Direct Nuclear Reactions*; Academic Press, Inc.: London, UK, 1983.

26. Cage, M.; Cole, A.; Pyle, G. Ambiguities and systematics in the real central part of the optical-model potential. *Nucl. Phys. A* **1973**, *201*, 418–432. [CrossRef]

27. Ohkubo, S.; Hirabayashi, Y. Evidence for a secondary bow in Newton's zero-order nuclear rainbow. *Phys. Rev. C* **2014**, *89*, 051601. [CrossRef]

28. Oliveira, J.R.B.; Cappuzzello, F.; Chamon, L.C.; Pereira, D.; Agodi, C.; Bondí, M.; Carbone, D.; Cavallaro, M.; Cunsolo, A.; De Napoli, M.; et al. Study of the rainbow-like pattern in the elastic scattering of ^{16}O on ^{27}Al at E$_{lab.}$= 100 MeV. *J. Phys. G Nucl. Part. Phys.* **2013**, *40*, 105101. [CrossRef]

29. Pereira, D.; Linares, R.; Oliveira, J.; Lubian, J.; Chamon, L.; Gomes, P.; Cunsolo, A.; Cappuzzello, F.; Cavallaro, M.; Carbone, D.; et al. Nuclear rainbow in the ^{16}O $+^{27}$Al system: The role of couplings at energies far above the barrier. *Phys. Lett. B* **2012**, *710*, 426–429. [CrossRef]

30. Cappuzzello, F.; Nicolosi, D.; Linares, R.; Oliveira, J.R.B.; Lubian, J.; Agodi, C.; Carbone, D.; Cavallaro, M.; de Faria, P.N.; Foti, A.; et al. Interplay of the elastic and inelastic channels in the ^{16}O + ^{27}Al scattering at E$_{lab.}$=280 MeV. *Eur. Phys. J. A* **2016**, *52*, 169. [CrossRef]

31. Zagatto, V.A.B.; Cappuzzello, F.; Lubian, J.; Cavallaro, M.; Linares, R.; Carbone, D.; Agodi, C.; Foti, A.; Tudisco, S.; Wang, J.S.; et al. Important role of projectile excitation in ^{16}O + ^{60}Ni and ^{16}O + ^{27}Al scattering at intermediate energies. *Phys. Rev. C* **2018**, *97*, 054608. [CrossRef]

32. Spatafora, A.; Cappuzzello, F.; Carbone, D.; Cavallaro, M.; Lay, J.A.; Acosta, L.; Agodi, C.; Bonanno, D.; Bongiovanni, D.; Boztosun, I.; et al. ^{20}Ne $+^{76}$Ge elastic and inelastic scattering at 306 MeV. *Phys. Rev. C* **2019**, *100*, 034620. [CrossRef]

33. Calabrese, S.; Cappuzzello, F.; Carbone, D.; Cavallaro, M.; Agodi, C.; Acosta, L.; Bonanno, D.; Bongiovanni, D.; Borello-Lewin, T.; Boztosun, I.; et al. First measurement of the ^{116}Cd(^{20}Ne,^{20}O)^{116}Sn reaction at 15 AMeV. *Acta Phys. Pol. B* **2018**, *49*, 275–280. [CrossRef]

34. Burrello, S. Analysis of two-step transfer mechanisms in ^{116}Cd (^{20}Ne, ^{20}F) ^{116}In at 306 MeV within the NUMEN project. in preparation.

35. La Fauci, L.; Spatafora, A.; Cappuzzello, F.; Agodi, C.; Carbone, D.; Cavallaro, M.; Lubian, J.; Acosta, L.; Amador-Valenzuela, P.; Borello-Lewin, T.; et al. ^{18}O+^{76}Se elastic and inelastic scattering at 275 MeV. *Phys. Rev. C* submitted.

36. Cavallaro, M.; Bellone, J.I.; Calabrese, S.; Agodi, C.; Burrello, S.; Cappuzzello, F.; Carbone, D.; Colonna, M.; Deshmukh, N.; Lenske, H.; et al. A constrained analysis of the ^{40}Ca(^{18}O,^{18}F)^{40}K direct charge exchange reaction mechanism at 275 MeV. *Front. Astron. Space Sci.* accepted.

37. Chamon, L.C.; Carlson, B.V.; Gasques, L.R.; Pereira, D.; De Conti, C.; Alvarez, M.A.G.; Hussein, M.S.; Cândido Ribeiro, M.A.; Rossi, E.S., Jr.; Silva, C.P. Toward a global description of the nucleus-nucleus interaction. *Phys. Rev. C* **2002**, *66*, 014610. [CrossRef]

38. Caminata, A.; Adams, D.; Alduino, C.; Alfonso, K.; Avignone, F.I.; Azzolini, O.; Bari, G.; Bellini, F.; Benato, G.; Bersani, A.; et al. Results from the Cuore Experiment. *Universe* **2019**, *5*, 10. [CrossRef]

39. Ebert, J.; Fritts, M.; Rajek, S.; Heidrich, N.; Neddermann, T.; Gehre, D.; Oldorf, C.; Quante, T.; Gopfert, T. Current Status and Future Perspectives of the COBRA Experiment. *Adv. High Energy Phys.* **2013**, *2013*, 703572. [CrossRef]

40. Barabash, A.; Belli, P.; Bernabei, R.; Cappella, F.; Caracciolo, V. Final results of the Aurora experiment to study 2β decay of ^{116}Cd with enriched ^{116}CdWO$_4$ crystal scintillators. *Phys. Rev. D* **2018**, *98*, 092007. [CrossRef]

41. Sgouros, O.; Soukeras, V.; Pakou, A.; Patronis, N.; Zerva, K.; Keeley, N.; Strojek, I.; TrzciŃSKA, A.; Piasecki, E.; Rusek, K.; et al. Backward angle structure in the ^{20}Ne+^{28}Si quasielastic scattering. *Int. J. Mod. Phys. E* **2013**, *22*, 1350073. [CrossRef]

42. Belery, P.; Delbar, T.; Grégoire, G.; Grotowski, K.; Wall, N.S.; Kozik, T.; Micek, S. Elastic scattering of ^{20}Ne+^{24}Mg at $E_{lab} = 50, 60, 80, 90,$ and 100 MeV. *Phys. Rev. C* **1981**, *23*, 2503–2512. [CrossRef]

43. Palumbo, A.; Tan, W.P.; Best, A.; Couder, M.; Crowter, R.; de Boer, R.J.; Falahat, S.; LeBlanc, P.J.; Lee, H.Y.; Strandberg, E. Systematic study of the α-optical potential via elastic scattering near the $Z = 50$ region for p-process nuclei. *Phys. Rev. C* **2012**, *85*, 035808. [CrossRef]

44. De, T.K.; Goswami, A.; Baliga, B.B. Scattering of alpha-particles from ^{130}Te at 40 and 50 MeV. *Il Nuovo Cimento* **1990**, *103A*, 1427–1434. [CrossRef]

45. Chen, X.; Lui, Y.W.; Clark, H.; Tokimoto, Y.; Youngblood, D. Folding model analysis of 240-MeV Li-6 elastic scattering on Sn-116 and inelastic scattering to low-lying states of Sn-116. *Phys. Rev. C* **2007**, *76*, 054606. [CrossRef]

46. Robertson, B.C.; Sample, J.T.; Goosman, D.R.; Nagatani, K.; Jones, K.W. Elastic Scattering of ^{16,18}O by ^{116,120}Sn at Energies near the Coulomb Barrier. *Phys. Rev. C* **1971**, *4*, 2176–2180. [CrossRef]

47. Rifuggiato, D.; Calabretta, L.; Celona, L.; Chines, F.; Cosentino, L.; Cuttone, G.; Finocchiaro, P.; Pappalardo, A.; Re, M.; Rovelli, A. Radioactive ion beam facilities at INFN LNS. *J. -Phys. Conf. Ser.* **2011**, *267*, 012007. [CrossRef]

48. Cavallaro, M.; Santagati, G.; Cappuzzello, F.; Carbone, D.; Linares, R.; Torresi, D.; Acosta, L.; Agodi, C.; Bonanno, D.; Bongiovanni, D.; et al. Charge-state distributions of ^{20}Ne ions emerging from thin foils. *Results Phys.* **2019**, *13*, 102191. [CrossRef]

49. Cappuzzello, F.; Carbone, D.; Cavallaro, M.; Cunsolo, A. MAGNEX: An innovative large acceptance magnetic spectrometer for nuclear reaction studies. In *Magnets: Types, Uses and Safety*; Akitsu, T., Ed.; Nova Science Publishers, Inc.: New York, NY, USA, 2011.

50. Cappuzzello, F.; Agodi, C.; Carbone, D.; Cavallaro, M. The MAGNEX spectrometer: Results and perspectives. *Eur. Phys. J. A* **2016**, *52*, 167. [CrossRef]

51. Cavallaro, M.; Cappuzzello, F.; Carbone, D.; Cunsolo, A.; Foti, A.; Khouaja, A.; Rodrigues, M.; Winfield, J.; Bondì, M. The low-pressure focal plane detector of the MAGNEX spectrometer. *Eur. Phys. J. A* **2012**, *48*, 59. [CrossRef]

52. Torresi, D.; Sgouros, O.; Soukeras, V.; Cavallaro, M.; Cappuzzello, F.; Carbone, D.; Agodi, C.; Brischetto, G.; Calabrese, S.; Ciraldo, I.; et al. An upgraded focal plane detector for the MAGNEX spectrometer. *Nucl. Instrum. Methods Phys. Res. Sect. A Accel. Spectrometer Detect. Assoc. Equip.* **2021**, *989*, 164918. [CrossRef]

53. Cappuzzello, F.; Cavallaro, M.; Cunsolo, A.; Foti, A.; Carbone, D.; Orrigo, S.; Rodrigues, M. A particle identification technique for large acceptance spectrometers. *Nucl. Instrum. Methods Phys. Res. Sect. A Accel. Spectrometers Detect. Assoc. Equip.* **2010**, *621*, 419–423. [CrossRef]

54. Cappuzzello, F.; Agodi, C.; Bondì, M.; Carbone, D.; Cavallaro, M.; Cunsolo, A.; De Napoli, M.; Foti, A.; Nicolosi, D.; Tropea, S.; et al. A broad angular-range measurement of elastic and inelastic scatterings in the ^{16}O on ^{27}Al reaction at 17.5 MeV/u. *Nucl. Instrum. Methods Phys. Res. Sect. A Accel. Spectrometer Detect. Assoc. Equip.* **2014**, *763*, 314–319. [CrossRef]

55. Carbone, D. Signals of the Giant Pairing Vibration in ^{14}C and ^{15}C nuclei populated by (^{18}O,^{16}O) two-neutron transfer reactions. *Eur. Phys. J. Plus* **2015**, *130*, 143. [CrossRef]

56. Cappuzzello, F.; Carbone, D.; Cavallaro, M. Measuring the ions momentum vector with a large acceptance magnetic spectrometer. *Nucl. Instruments Methods Phys. Res. Sect. A Accel. Spectrometers, Detect. Assoc. Equip.* **2011**, *638*, 74–82. [CrossRef]

57. Cavallaro, M.; Cappuzzello, F.; Carbone, D.; Cunsolo, A.; Foti, A.; Linares, R. Transport efficiency in large acceptance spectrometers. *Nucl. Instruments Methods Phys. Res. Sect. A Accel. Spectrometers, Detect. Assoc. Equip.* **2011**, *637*, 77–87. [CrossRef]

58. Thompson, I.J. Coupled reaction channels calculations in nuclear physics. *Comput. Phys. Rep.* **1988**, *7*, 167–212. [CrossRef]

59. Crema, E.; Otomar, D.; Simoes, R.; Barioni, A.; Monteiro, D.; Ono, L.; Shorto, J.; Lubian, J.; Gomes, P. Near-barrier quasielastic scattering as a sensitive tool to derive nuclear matter diffuseness. *Phys. Rev. C* **2011**, *84*, 024601. [CrossRef]

60. Crema, E.; Zagatto, V.A.B.; Shorto, J.M.B.; Paes, B.; Lubian, J.; Simões, R.F.; Monteiro, D.S.; Huiza, J.F.P.; Added, N.; Morais, M.C.; et al. Reaction mechanisms of the ^{18}O $+^{63}$Cu system at near-barrier energies. *Phys. Rev. C* **2018**, *98*, 044614. [CrossRef]

61. Fonseca, L.M.; Linares, R.; Zagatto, V.A.B.; Cappuzzello, F.; Carbone, D.; Cavallaro, M.; Agodi, C.; Lubian, J.; Oliveira, J.R.B. Elastic and inelastic scattering of ^{16}O on ^{27}Al and ^{28}Si at 240 MeV. *Phys. Rev. C* **2019**, *100*, 014604. [CrossRef]

62. Alvarez, M.A.G.; Chamon, L.C.; Hussein, M.S.; Pereira, D.; Gasques, L.R.; Rossi, E.S., Jr.; Silva, C.P. A parameter-free optical potential for the heavy-ion elastic scattering process. *Nuclear Physics A* **2003**, *723*, 93–103. [CrossRef]

63. Khoa, D.T.; Satchler, G. Generalized folding model for elastic and inelastic nucleus–nucleus scattering using realistic density dependent nucleon–nucleon interaction. *Nucl. Phys. A* **2000**, *668*, 3–41. [CrossRef]

64. Chamon, L.; Carlson, B. Systematics of nuclear densities, deformations and excitation energies within the context of the generalized rotation–vibration model. *Nucl. Phys. A* **2010**, *846*, 1–30. [CrossRef]

65. Pritychenko, B.; Birch, M.; Singh, B.; Horoi, M. Tables of E2 transition probabilities from the first 2+ states in even–even nuclei. *At. Data Nucl. Data Tables* **2016**, *107*, 1–139. [CrossRef]

66. Raman, S.; Nestor, C., Jr.; Tikkanen, P. Transition probability from the ground to the first-excited 2$^+$ state of even–even nuclides. *At. Data Nucl. Data Tables* **2001**, *78*, 1. [CrossRef]

67. Jonsson, N.G.; Bäcklin, A.; Kantele, J.; Julin, R.; Luontama, M.; Passoja, A. Collective states in even Sn nuclei. *Nucl. Phys. A* **1981**, *371*, 333–348. [CrossRef]

68. Bäcklin, A.; Jonsson, N.; Julin, R.; Kantele, J.; Luontama, M.; Passoja, A.; Poikolainen, T. 0+ states and E0 and E2 transition rates in even Sn nuclei. *Nucl. Phys. A* **1981**, *351*, 490–508. [CrossRef]

69. Thompson, I.J.; Nagarajan, M.A.; Lilley, J.S.; Smithson, M.J. The threshold anomaly in ^{16}O + ^{208}Pb scattering. *Nucl. Phys. A* **1989**, *505*, 84. [CrossRef]

70. Rangel, J.; Lubian, J.; Canto, L.F.; Gomes, P.R.S. Effect of Coulomb breakup on the elastic cross-section of the ^{8}B proton-halo projectile on a heavy, ^{208}Pb target. *Phys. Rev. C* **2016**, *93*, 054610. [CrossRef]